Supporting Information

A local Proton–Transport Promoter for Industrial and Selective CO_2 Electroreduction to Multicarbon Products

Haiyi Guo[a], Huang Qi[a], Di Li[a], Shiyu Dai[b], Kang Yang[a], Sheng Chen[a], Wei Ma[b]* Qiang Li[a]* and Jingjing Duan[a]*

[a]MIIT Key Lab Thermal Control Electronic Equipment, School of Energy and Power Engineering, School of Chemistry and Chemical Engineering, Nanjing University of Science and Technology, Nanjing, 210094, China

[b]Key Laboratory for Advanced Materials and Joint International Research Laboratory of Precision Chemistry and Molecular Engineering, Frontiers Science Center for Materiobiology and Dynamic Chemistry, School of Chemistry and Molecular Engineering, East China University of Science and Technology, Shanghai 200237, P. R. China

Experimental Section

Materials and Chemicals

Pyrrole (C_4H_5N) was purchased from Maclean (China). Thiophene (C_4H_4S), ammonium persulfate ($(NH_4)_2S_2O_8$), absolute ethanol (C_2H_5OH) and dimethylsulfoxide (DMSO, ≥99.8%) were purchased from Aladdin (China). Hydrazine hydrate ($N_2H_4 \cdot H_2O$), copper chloride dihydrate ($CuCl_2 \cdot 2H_2O$), trisodium citrate dihydrate ($C_6H_5Na_3O_7 \cdot 2H_2O$), potassium hydroxide (KOH) and isopropyl alcohol (IPA) were purchased from Sinopharm Chemical Reagent Co. Ltd (China). D_2O (99.9 atom %D) was purchased from Acros Organics.

Synthesis of Polypyrrole (PPy)

0.1 ml pyrrole and 1.444 mmol ammonium persulfate were dissolved separately in 10 ml and 20 ml deionized water (DI) with ice bath stirring for 20 min. Then, the pre-prepared ammonium persulfate solution was added slowly as an oxidant to the pyrrole solution and stirred in ice-bath for 6 h. After the reaction, the dark precipitate was washed with deionized water and ethanol repeatedly by centrifugation, and then freeze-dried for 24 h.

Synthesis of Polythiophene (PTh)

0.2 ml thiophene and 2.534 mmol ammonium persulfate were dissolved in 30 ml deionized water with magnetic stirring for 30 min to form uniform dispersion. Then, dispersion was transferred to a Teflon-lined stainless-steel autoclave and kept at 90℃ for 24 h. After cooling down, the brownish black precipitate was washed with deionized water and ethanol repeatedly by centrifugation, and then freeze-dried for 24 h.

Synthesis of Copper/Polymer Hybrids

40 mg PPy powder was dispersed in 40 ml deionized water and stirred vigorously until well-dispersed. Then, 71.55 mg copper chloride dihydrate and 400 mg trisodium citrate dihydrate were dissolved to the dispersion and agitated for 30 min, until homogeneous dark green color was

achieved. The mixture was heated to 60℃ in a water bath, then 1 ml hydrazine hydrate added, and kept stirred for another 30 min. The final product was washed by centrifugation with deionized water and ethanol respectively, and then freeze-dried for 24 h.

Synthesis of Copper/Polymer Hybrids gas diffusion electrodes

YLS-30T carbon paper with hydrophobic microporous layer, which has good hydrophobicity, is used as the gas diffusion layer of the cathode in this paper. The electrodes were prepared by spraying catalyst dispersion, and the preparation process was as follows: First cut the carbon paper to a square size of 3 × 3 cm^2 to cover the alkaline flow cell chamber, and soaked in 0.1 M hydrochloric acid, deionized water, and ethanol for 10 min each to remove the surface impurities of the carbon paper. The carbon paper was soaked in 0.1 M hydrochloric acid, deionized water and ethanol for 10 min to remove trace impurities from the surface of the carbon paper, and then dried in a vacuum drying oven for 24 h. PTFE emulsion was applied to the large pore layer on the back of the carbon paper and sintered at 300 °C for 1.5 h in a muffle furnace to improve the hydrophobicity of the carbon paper; the conventional catalyst dispersion consisted of 10 mg of solid catalyst, 250 μL of deionized water, 710 μL of isopropanol and The conventional catalyst dispersion consisted of 10 mg of solid catalyst, 250 μL of deionized water, 710 μL of isopropanol and 40 μL of membrane solution Nafion (5 wt%) for 1 h to obtain a homogeneous catalyst dispersion. Prepared carbon paper is placed on a heated table at 70℃, and the exposed area of carbon paper is controlled using a custom mold. at 1 × 1 cm^2 by using a custom mold, and the dispersion was sprayed onto the exposed surface of the carbon paper using an airbrush. After the catalyst was fully dried, the mass of the carbon paper was repeatedly weighed before and after spraying, and the loading of the catalyst was controlled at 1 mg/cm^2. Finally, the carbon paper was prepared as cathode working electrode by using copper conductive tape and insulating tape. Nickel foam has a good pore structure to provide reaction area and good oxygen precipitation reaction (OER) activity. In this paper, commercial nickel foam treatment with 110 ppi porosity and 0.5 mm thickness was used as the anode in this paper. The reference electrode was a Ag/AgCl electrode.

Details of eCO_2RR testing

The eCO_2RR performance of cathode Cu/PPy, Cu/PTh catalysts was tested using a homemade flow cell. The reference electrode was a $Ag/AgCl$ electrode, the counter electrode was nickel foam, and the ion exchange membrane was an anion exchange membrane. The flow cell consists of three chambers: an anodic liquid chamber, a cathodic liquid chamber and a gas flow chamber. The gas diffusion electrode (GDE) is sandwiched between the cathodic liquid chamber and the gas flow chamber, with the substrate side facing the gas flow chamber and the catalyst side facing the anion chamber. The anion exchange membrane (AEM) was sandwiched between the cathode and anode chambers. The anion solution and cation exchange membrane in all experiments were 20 ml and 20 ml of 1 M KOH aqueous solution, respectively, and all potentials were uncorrected. All potentials are uncorrected for iR loss. All applied potentials were calculated for RHE according to the following equation:

$$V_{RHE} = Vv_{ersus\ Ag/AgCl} + 0.059 \times pH + 0.197 \quad (1)$$

Liquid products were quantified using nuclear magnetic resonance spectroscopy (NMR). The yields of the liquid products were accurately detected and quantified using 10 mmol/L DMSO as an internal standard for NMR detection. Gaseous products are collected in gas bags and pump to GC,1 mL of CO_2RR gas product was analyzed using a gas chromatograph (GC, Agilent 8890) equipped with a thermal conductivity detector (TCD) and a flame ionization detector (FID).

Causes of FE loss at high current density of ~800mA cm^{-2}: Firstly, when CO_2 is dissolved in alkaline electrolyte, the electrode surface produces numerous gas bubbles. Therefore, some of the gas phase products will enter the cathode chamber electrolyte and leak from the electrolyte without being completely collected for analysis in gas chromatography (*Nature Communications, 2023, 14(1): 1158*), resulting in the loss of total Faraday efficiency. Secondly, the liquid product is not fully detected because it passes through the gas diffusion layer and the ion exchange membrane (*Journal of catalysis, 2020, 385: 140-145*), resulting in a total FE of only ~80% at the current density >800 mA/cm^2.

Characterizations

X-ray diffraction (XRD) patterns were acquired with a X-ray diffractometer (Bruker D8 ADVANCE, Germany) using Cu Kalpha radiation. The structures and morphology were characterized by field emission scanning electron microscopy (FESEM, GeminiSEM 300, Germany) equipped with energy dispersive X-ray spectroscopy (EDS). The surface elemental composition and chemical states were measured using X-ray photoelectron spectroscopy (XPS, Thermo Scientific K-Alpha, America) with an Al Kalpha X-ray source. CO_2 adsorption isotherms measurements were carried out by using an automatic microporous physical and chemical gas adsorption analyzer (ASAP2020, America).

DFT details

DFT calculations were performed by the MedeA-Vienna Ab initio Simulation Package (VASP). The GGA-rPBE generalized gradient approach was used to define the exchange-correlation potential.[1, 2] The interaction between the atomic cores and electrons was described by using the projector augmented wave method (PAW).[3, 4] The plane wave energy cutoff was set to be 400 eV. The Brillouin zone in the real space was sampled with a 2 × 2 × 1 Monkhorst-Pack K-point grid. The convergence criterion was set to be 10-5 eV and 0.05 eV/Å for energy and force in the geometry optimizations, respectively. A Gaussian smearing method was employed with 0.1 eV width. Hubbard-U correction method (DFT+U) was carried out to improve the description of highly correlated Cu 3d orbitals with the value of U-J set to be 2.5 eV.

The detailed Gibbs free energy has been calculated according to the following equation:

$$G = E + ZTE - TS + G_{pH} + eU \qquad (2)$$

Where G, E and ZTE refer to chemical Gibbs free energy, electronic energy and zero-point energy, respectively. G_{pH} is the free energy correction of pH, and can be calculated by:

$$G_{pH}=K_BT\times pH\times \ln 10 \qquad (3)$$

Notably, the pH value was set to be zero and fourteen in this work; U was the applied potential.[5] The entropy can be calculated by the sum of the vibrational, rotational, translational, and electronic

contribution as to:

$$S = S_v + S_r + S_t + S_e \quad (4)$$

Since $S_e \approx 0$ at the fundamental electronic level.

For the case of solids and adsorbates, some approximations can be adopted: Translational and rotational motions can be omitted, therefore, $S_t \approx 0$ and $S_r \approx 0$. In this case, all the entropy values come from the vibrational contribution: $S=S_v$.

Finally, Gibbs free energy for different states was calculated as to:

$$G = E + ZTE - TS_v + G_{pH} + eU \quad (5)$$

Durability measurements

Durability was measured using a FLOW-CELL device with 1M KOH as the electrolyte. The catalyst area was 0.5cm^2 and the test was conducted at a constant current of 100mA.

Four-electrode AC impedance model

To exclude the interference of GDL conductivity, we use an insulating substrate-loaded catalyst layer to improve the impedance signal-to-noise ratio. We pressed four silver wires as electrodes on the surface of the catalyst layer, applied an alternating current to the surface of the catalyst layer through the outer silver wire electrodes, and then collected the voltage drop across the intermediate silver wires, the four-electrode method can exclude the interference of the external impedance of the catalyst layer[6]. The experiments were conducted to reduce the catalyst layer in a wetted state, and the catalyst layer was wetted with deionized water prior to testing and removed so that there were no visible water droplets on the surface, and the default catalyst layer humidity was a maximum of 98% RH. The AC impedance method was used to characterize the temperature-dependent dual conductivity of the polymers, and the instrument was a Chenhua 760e electrochemical workstation. The impedance spectra were tested at different temperatures (40°C, 50°C, 60°C, 70°C, 80°C), stabilised for at least 10 min at each temperature prior to the test and the test was repeated twice, with the impedance test frequency ranging from 100 KHz-1 Hz.

The system can be viewed as a parallel connection of an electronic impedance element and an ionic impedance element, and the low-frequency AC current is equivalent to a DC voltage driving the electronic operation. The low-frequency AC current is equivalent to a DC voltage driving the electrons, and the equivalent circuit can be regarded as the only electronic impedance element. In the case of high-frequency AC, both electrons and ions can move back and forth under AC voltage. In the case of high-frequency AC, both electrons and ions can move back and forth under the AC voltage, and the measured impedance includes both electronic and ionic transfer parts. The equivalent circuit can be seen as a parallel connection of the ionic impedance and the electronic impedance (**Fig. S23b**). The corresponding formula for calculating conductivity is given below:

$$\sigma = \frac{L}{\omega \times t \times R} \quad (6)$$

where σ is the electrical conductivity (S/cm or mS/cm); L is the distance between the two silver wire electrodes; ω is the width of the catalyst layer (cm); t is the thickness of the catalyst layer (cm, observed by SEM); R is the impedance (Ω, derived by fitting the equivalent circuit); the high-frequency impedance includes both the ionic and electronic impedance components:

$$R_{ionic} = \frac{1}{\frac{1}{R_{high}} - \frac{1}{R_{electronic}}} \quad (7)$$

where $R_{electronic}$ is the electronic impedance (Ω, equal to the low frequency impedance R_{low}); R_{high} is the high frequency impedance (Ω); R_{ionic} is the ionic impedance (Ω, from Equation 6). Arrhenius equation

$$\sigma = \sigma_0 exp\left(-\frac{E_a}{k_B T}\right) \quad (8)$$

where σ is the electronic conductivity (S/cm); σ_0 is the prefactor; E_a is the thermal activation energy (eV); k_B is the Boltzmann constant; T is the absolute temperature (K).

$$\sigma T = A exp\left(-\frac{E_a}{k_B T}\right) \quad (9)$$

where σ is the proton conductivity (S/cm); T is the absolute temperature (K); A is the the pre-exponential factor.; E_a is the activation energy for proton conductivity (eV); k_B is the Boltzmann

constant.

MD Simulation details

All the MD simulations were performed by using the Accelrys Materials Studio 7.0 software package.The simulation box was generated by a random distribution of polymer chains consisting of 20 conductive polymer monomers. These polymer chains are individually energy-minimized and geometrically optimized before the simulated boxes are created. Energy minimization and geometric optimization are performed by conjugate gradient method.

The simulations were performed at 298 K and a periodic boundary condition with an initial density of 0.8 g/cm^3. The initial configuration of the simulation box is first minimized to reduce energy and eliminate overlaps and close contacts. And then the structure in the simulated box is geometrically optimized. After completing these steps, the cell density and energy remain constant, indicating that the system has reached equilibrium. After equilibration, the production run was performed at 298 K for 500 ps NVT. All MD simulations were performed by using the Ewald summation method[7, 8] with a fine accuracy of 1.0e-5kcal/mol for both equilibrium phases and production runs. Nose thermostats and barometers are used to control the temperature and pressure in the simulation process[9]. During the MD simulation, the time step of the NVT ensemble was 1.0 fs.

Force field. The COMPASS (Condensed Phase Optimized Molecular Potential for Atomistic Simulation Studies) force field[10] is widely acknowledged for its effectiveness in modeling interactions, particularly in the fields of molecular dynamics and ab initio simulations.The total potential energy in this force field is given by the following equation:

$$E_{total} = E_{valence} + E_{crossterm} + E_{non-bonded}$$

$$= E_b + E_\theta + E_\phi + E_\chi + E_{bb'} + E_{b\theta} + E_{b\phi} + E_{\theta\theta'} + E_{\theta\theta'\phi} + E_{elec} + E_{LJ} \quad (10)$$

where the valence term $E_{valence}$ denotes molecular interactions which includes: bond (E_b), angle (E_θ), torsion (E_ϕ) and out of plane angle (E_χ). The cross-coupling term $E_{crossterm}$ in Equation (1) includes the following interactions terms: bond-bond ($E_{bb'}$), bond-angle ($E_{b\theta}$), bond-torsion ($E_{b\phi}$),

angle-angle ($E_{\theta\theta'}$) and angle-angle-torsion ($E_{\theta\theta',\phi}$). The cross-coupling term $E_{crossterm}$ is important for predicting vibrational frequencies and structural changes associated with conformational changes. The non-bonded term $E_{non\text{-}bonded}$, includes the electronic interaction (E_{elec}), which is represented by Coulombic and Lenard-Jones 9-6 (E_{LJ}) potential for the vander Waals (vdW) interactions.

Mean square displacement (MSD). The diffusion coefficient is related to the vehicular mechanism, and the water diffusion coefficient (D) can be calculated from the mean-square displacement (MSD) and Einstein's diffusion equation in the following forms[11]:

$$MSD = \{[R(t) - R(0)]^2\} \quad (11)$$

$$D = \frac{1}{6}\lim_{t\to\infty}\left\langle\left\{\frac{[R(t) - R(0)]^2}{t}\right\}\right\rangle = \frac{1}{6}lim\frac{dMSD}{dt} \quad (12)$$

where R(t) and R(0) are the positions to which the species (water and hydrated hydrogen ions) diffuse at time t and initial time (t=0) of the MD simulation, respectively. The relationship between the conductivity and diffusion coefficient (D) of water molecules and hydrated hydrogen ions is expressed as:

$$\sigma = \frac{Dne^2}{kT} \quad (13)$$

where k, n, T and e are the Boltzmann constant, the number of molecules per cell volume, the Kelvin temperature and the elementary charge, respectively.

Radial distribution function (RDF). By evaluating the radial distribution function $g_{(A\text{-}B)}(r)$, it is possible to determine whether there is a molecular moiety from one cluster near another molecular moiety in a different cluster. This function represents the probability of finding an atom B at a distance r from atom A in the MD trajectory and is an average over all MD trajectories. The mathematical expression for this function is as follows[12, 13]:

$$g_{A-B} = \left(\frac{n_B}{4\pi r^2 \Delta r}\right) / \left(\frac{N_B}{V}\right) \quad (14)$$

where n_B is the number of atoms B located at distance r around atom A and in a shell of thickness Δr. N_B and V are the total number of atoms B and the total volume of the system,

respectively.

SECM Measurements

The SECM device is shown in **Fig. S27a**，it illustrates that the surface of Pt-UME is smooth enough for detection and radius of Pt is about 13 μm. RG (ratio of overall probe diameter to active electrode diameter) of the electrode is 3.4, which is suitable for SECM (Fig. S23b). Blank voltammetry (Fig. S23c) shows the expected voltammetric features of a clean polycrystalline platinum surface. The diffusion-limited steady-state current of Pt-UME (Fig. S23d) resulting from the FcMeOH/[FcMeOH]+ redox couple. The Pt-UME radius can be calculated through equation (14):

$$i = 4nFDCa \quad (15)$$

where i is diffusion-limited steady-state current (i=3.5 nA), n is the number of electrons transferred per molecule (n=1), F is the Faraday constant (F=96485 $Cmol^{-1}$), D is the diffusion coefficient of FcMeOH (D=6.67 × 10^{-10} m^2 s^{-1}), a is the radius of UME, and C is the concentration of FcMeOH (C=0.9 mM). The radius is calculated to be 13.3 μm, which is consistent with the optical size.

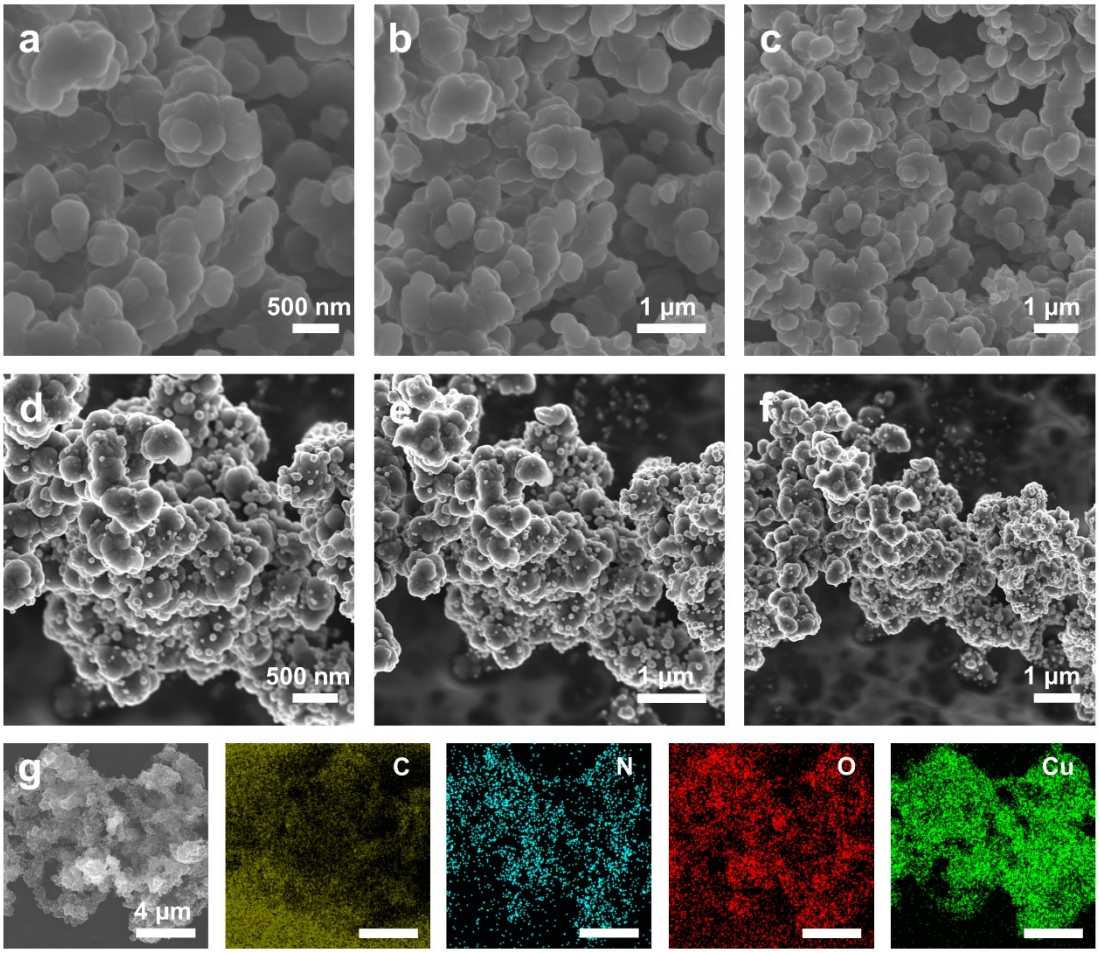

Fig. S1 (a-c) SEM images of pure PPy and (d-f) Cu/PPy; (g) SEM image of its EDS mapping images of C, N, O, Cu elements of Cu/PPy.

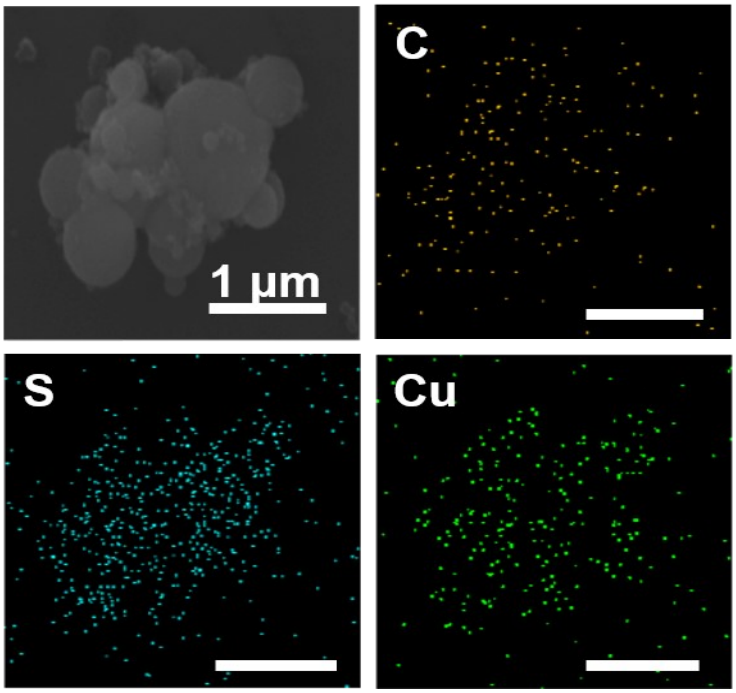

Fig. S2 SEM and its EDS images of C, S, Cu elements in Cu/PTh.

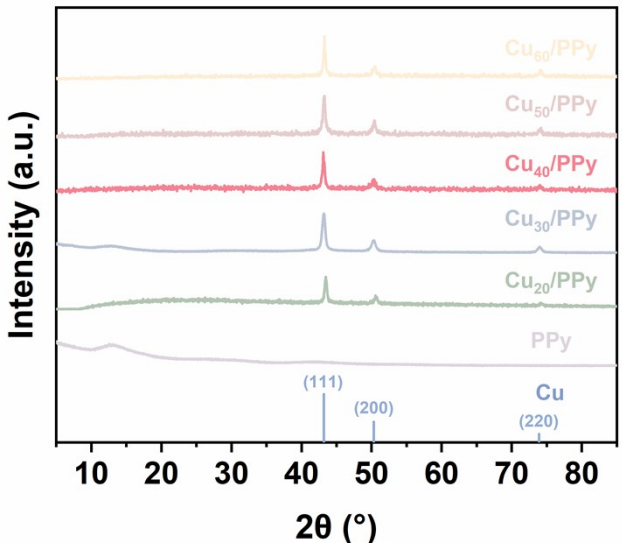

Fig. S3 XRD patterns of Cu/PPy composites with different Cu loadings.

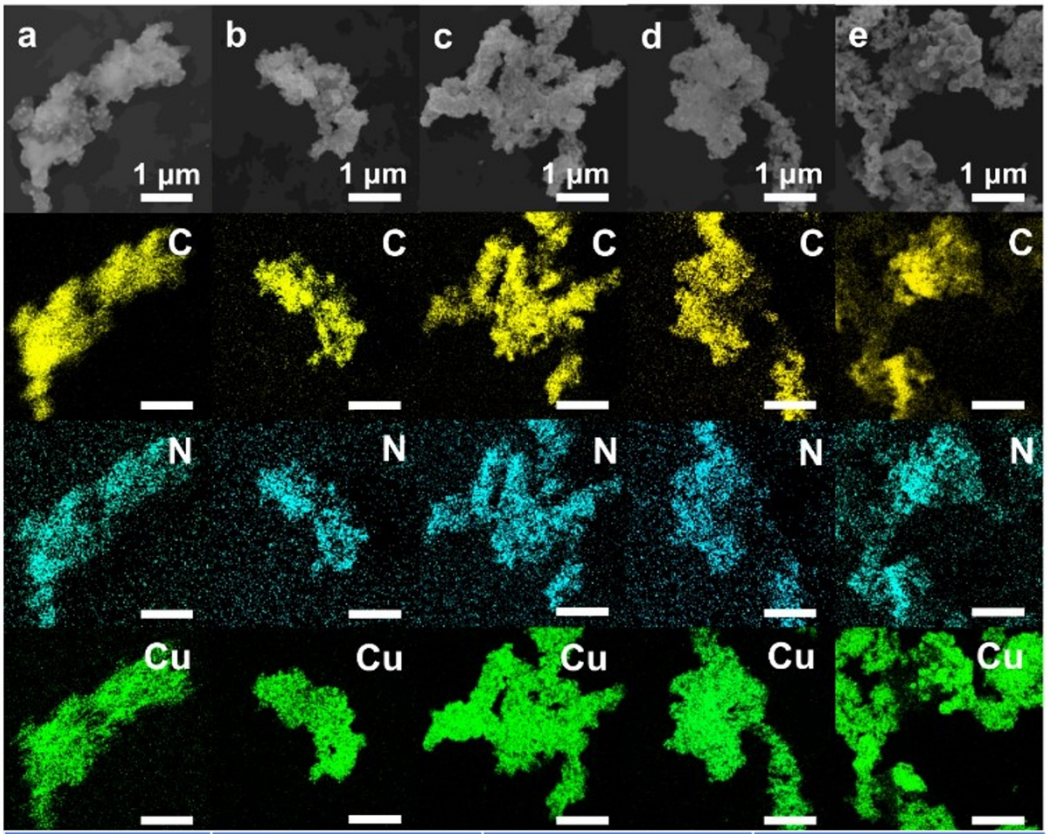

Fig. S4 SEM and the EDS mapping images of C, N and Cu elements in (a) Cu_{20}/PPy; (b) Cu_{30}/PPy; (c) Cu_{40}/PPy; (d) Cu_{50}/PPy; (e) Cu_{60}/PPy.

1 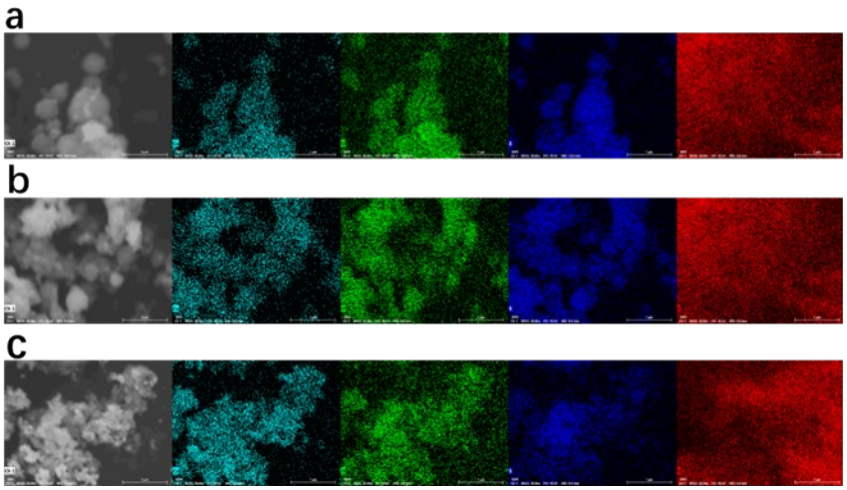

2 **Fig. S5** SEM and the EDS mapping images of Cu, O, S and C elements in (a) Cu_{20}/PTh; (b) Cu_{40}/PTh;

3 (c) Cu_{60}/PTh.

4

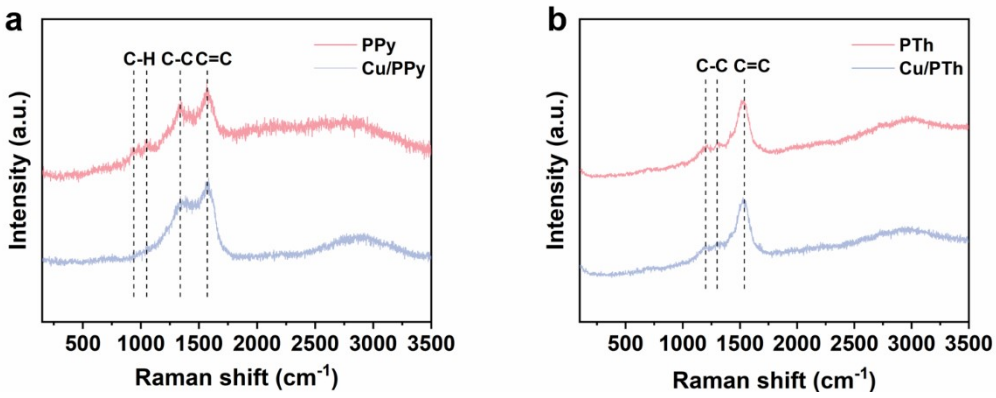

Fig. S6 Raman spectra of (a) PPy, Cu/PPy; (b) PTh and Cu/PTh.

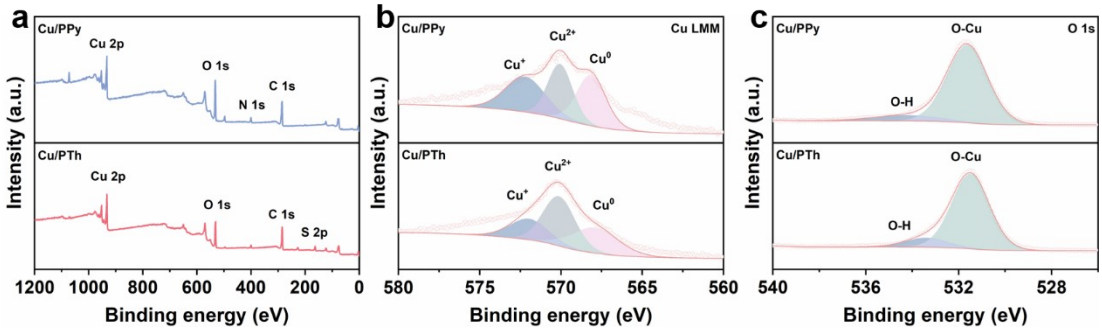

Fig. S7 XPS spectra of (a) the survey scan, (b) Cu LMM and (c) O 1s of Cu/PPy and Cu/PTh.

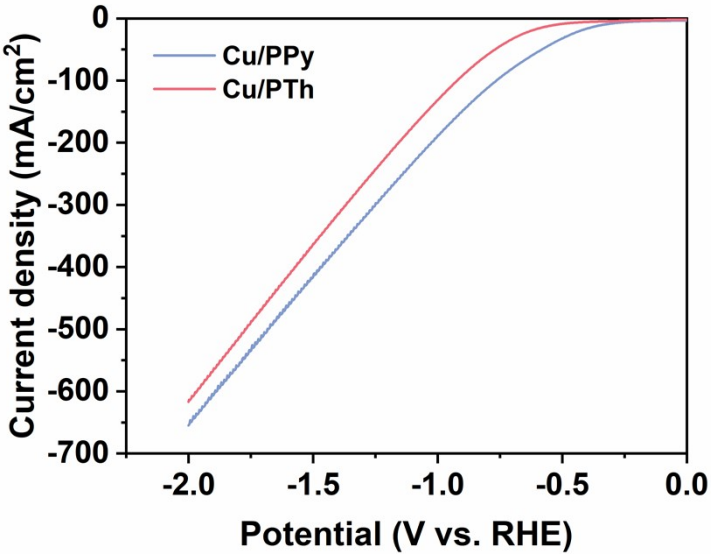

Fig. S8 Linear sweep voltammetry of Cu/PPy and Cu/PTh

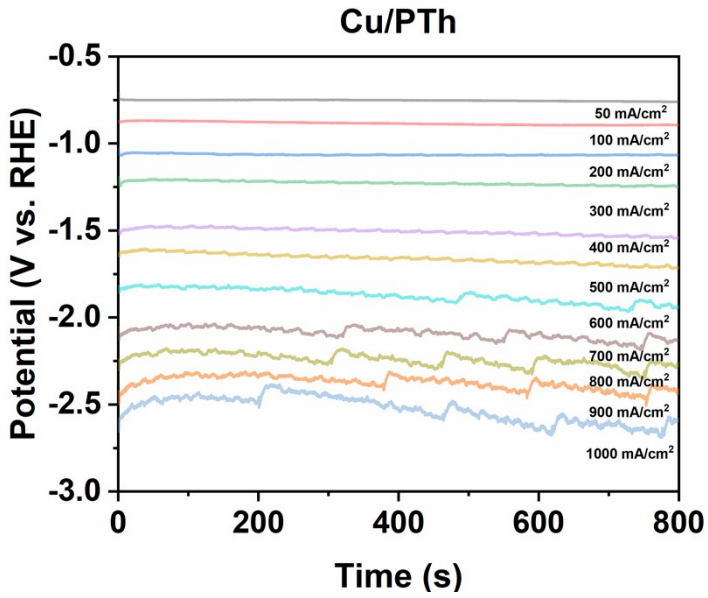

Fig. S9 The chronoamperometry testing of eCO_2RR promoted by Cu/PTh at the current density of 50, 100, 200, 300, 400, 500, 600, 700, 800, 900, 1000 mA cm^{-2}.

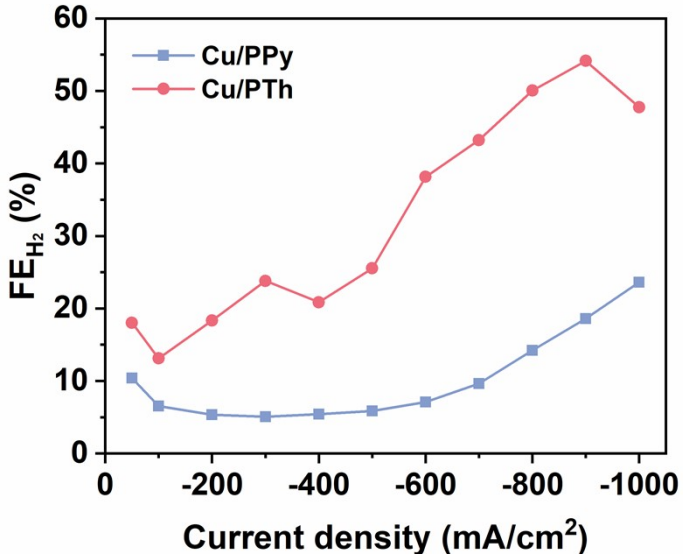

Fig. S10 Faraday efficiency of H_2 at different current densities.

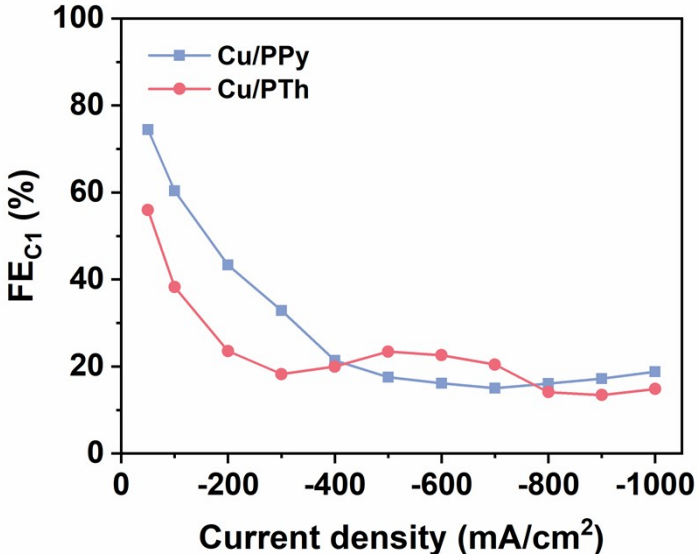

Fig. S11 Faraday efficiency of C_1 products at different current densities.

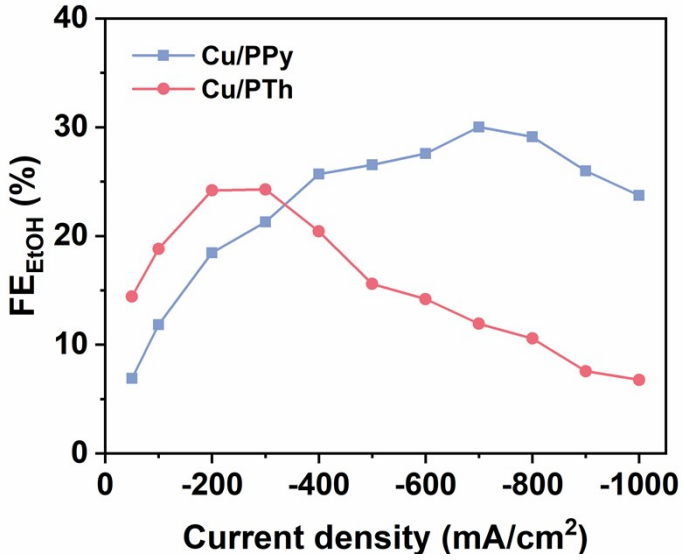

Fig S12 Faraday efficiency of the EtOH product at different current densities.

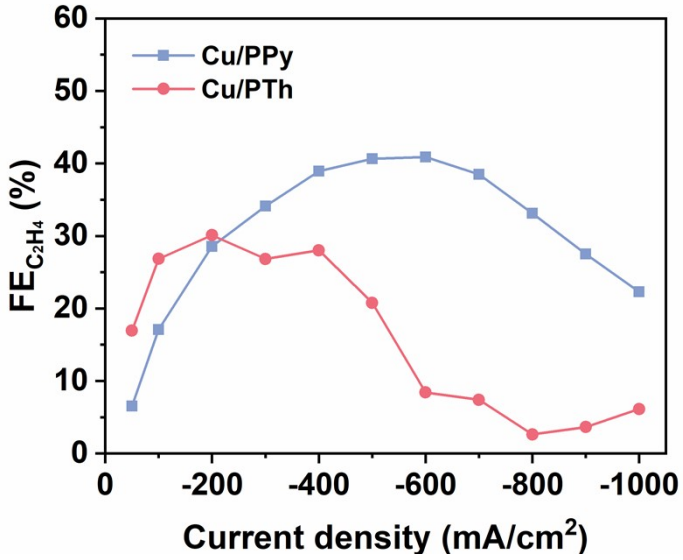

Fig. S13 Faraday efficiency of the C_2H_4 product at different current densities.

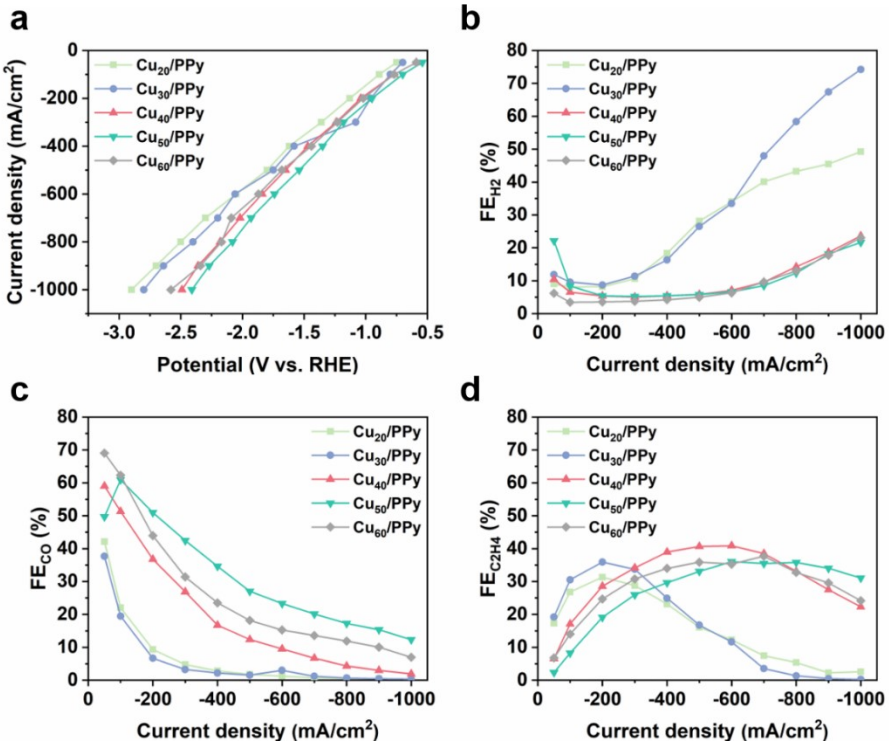

Fig. S14 (a) Polarization curves plotted using the steady-state current density and applied potentials; (b-d) Faraday efficiency of H_2, CO, C_2H_4 of eCO_2RR promoted by Cu_x/PPy electrodes.

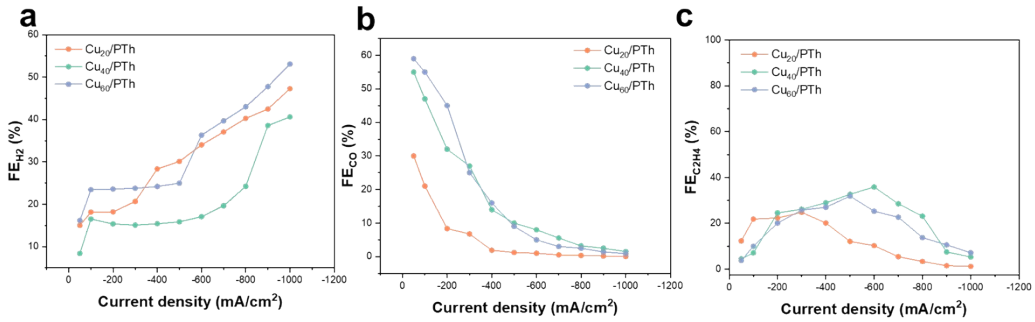

Fig. S15 (a-c) Faraday efficiency of H_2, CO, C_2H_4 of eCO_2RR promoted by Cu_x/PTh electrodes.

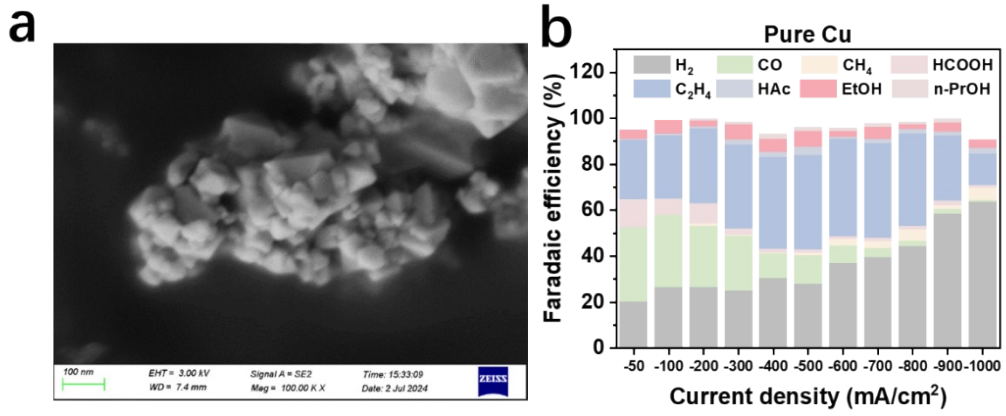

Fig. S16 (a) SEM images of Pure Cu; (b) CO_2 electroreduction performance of Cu.

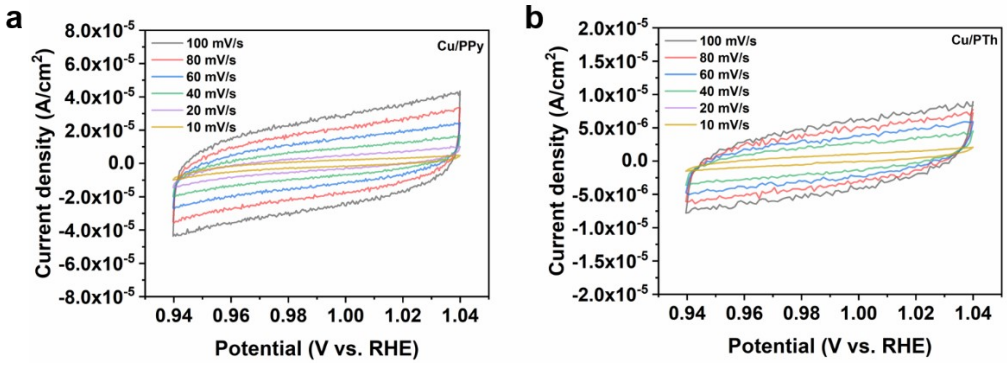

1

2 **Fig. S17** CV curves tested of in the range of 0.94 to 1.04 V (vs RHE) scanned using different sweep

3 speeds of eCO_2RR promoted using the Cu/PPy and Cu/PTh electrode.

4

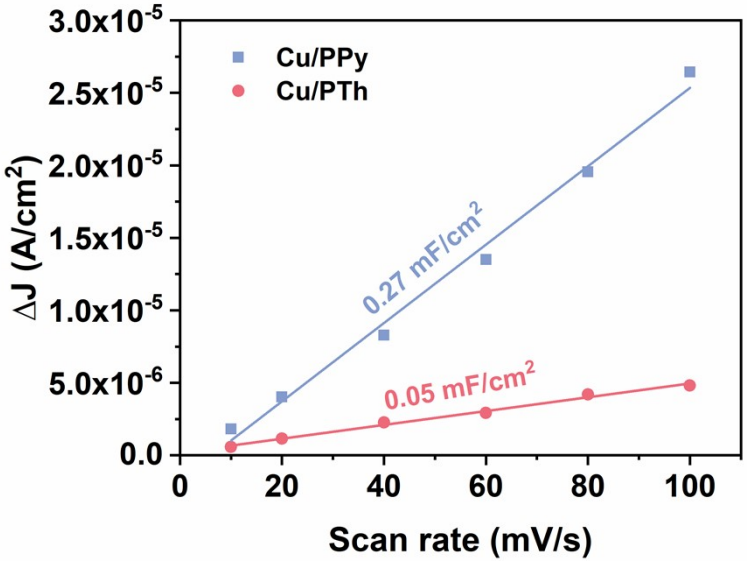

Fig. S18 Capacitance tested at different scan rates and the linear fitting for the eCO_2RR catalyzed by Cu/PPy and Cu/PTh.

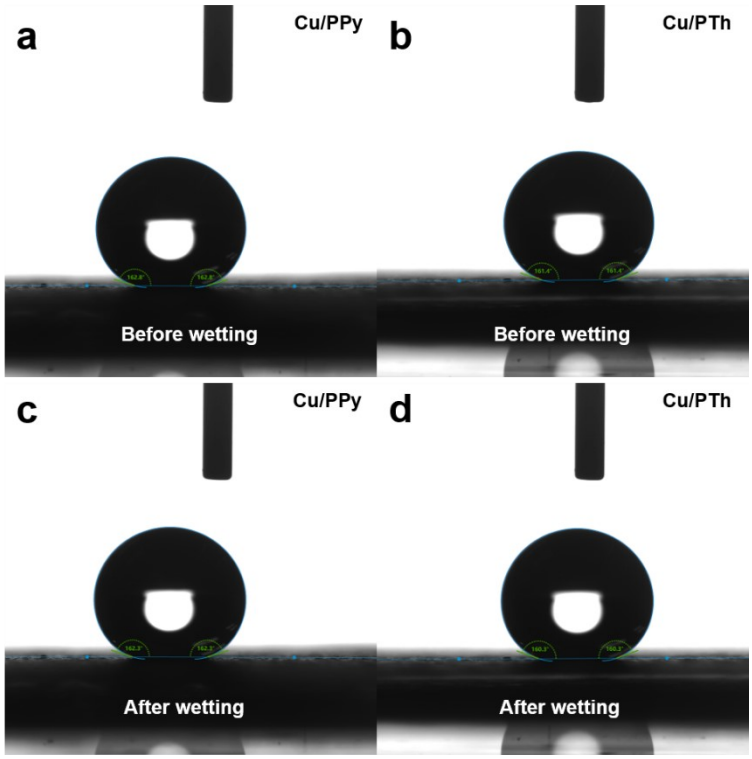

Fig. S19 Static contact angles before and after wetting of the Cu/PPy and Cu/PTh electrode.

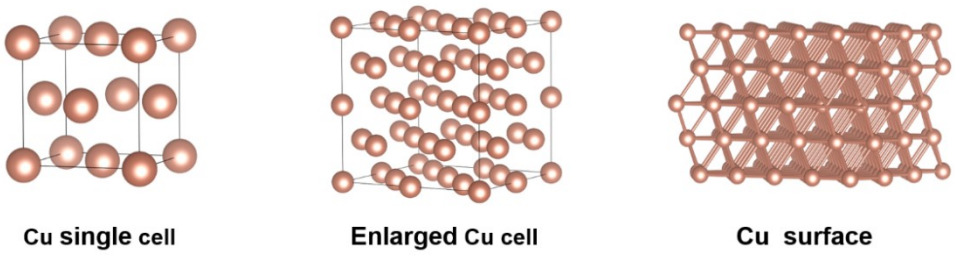

1

2 **Fig. S20** The configuration of crystal cells and the (111) surface of Cu crystals.

3

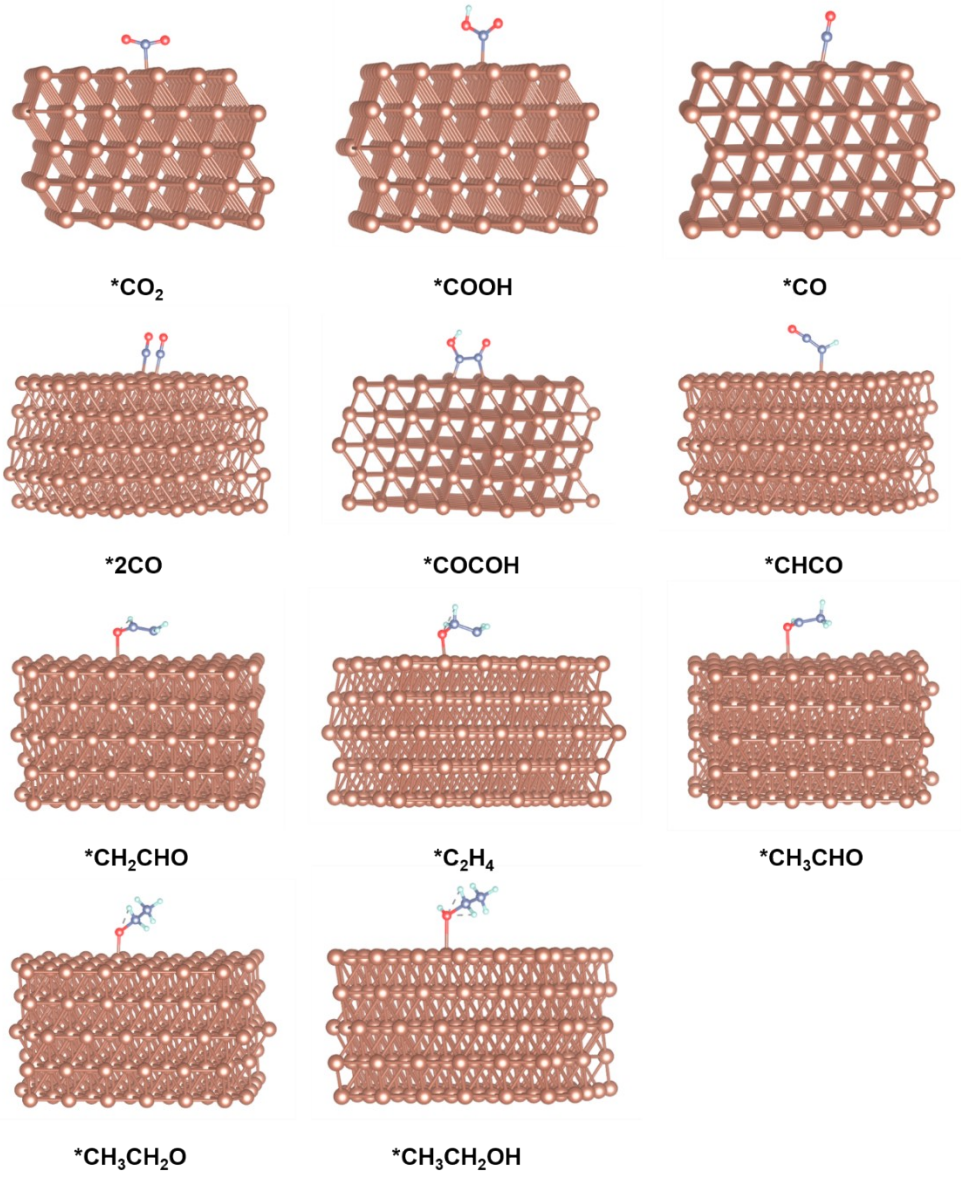

Fig. S21 Schematic diagrams of intermediates adsorbed on the Cu/PPy surface.

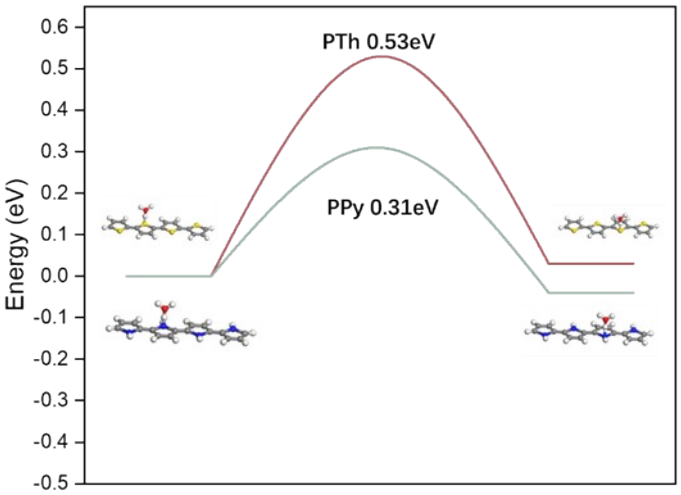

Fig. S22 Energy barriers of transition state for H_3O^+ jumping on PTh & PPy.

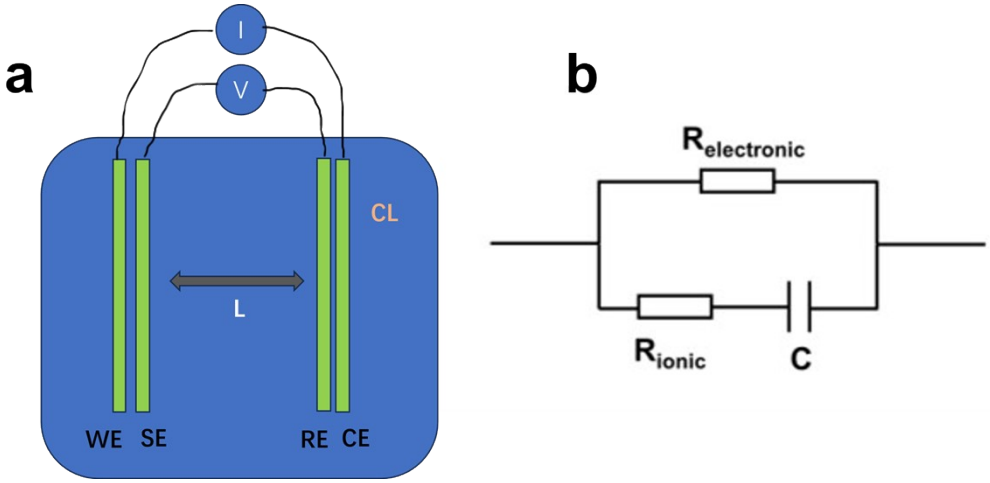

Fig. S23 (a) Schematic diagram of a four-electrode device; (b) A fitted equivalent circuit.

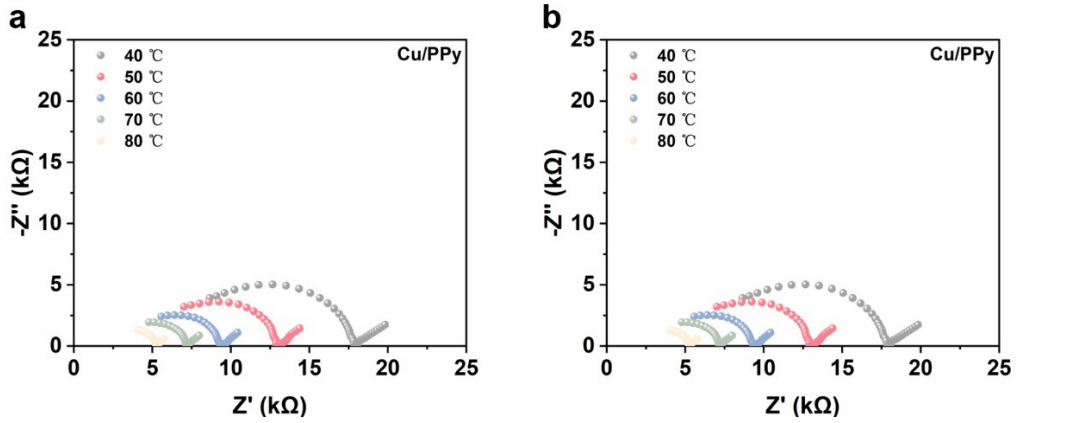

Fig. S24 Nyquist plots of eCO_2RR promoted by Cu/PPy and Cu/PTh tested at different temperatures.

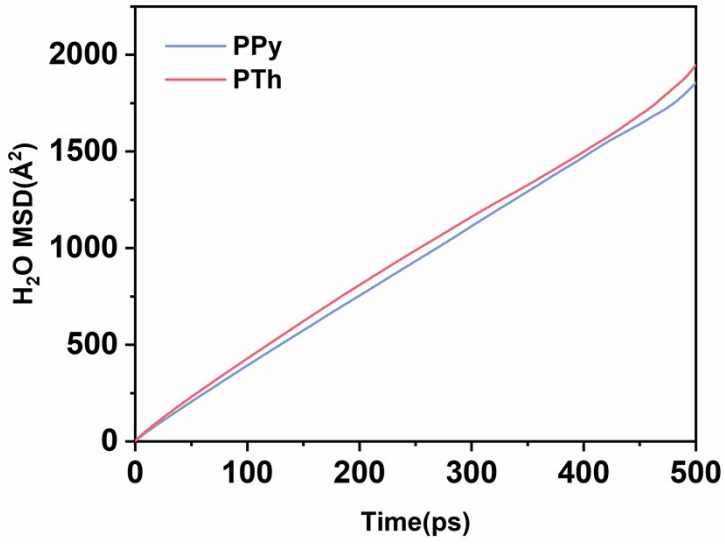

Fig. S25 MSD of the water molecule in the eCO_2RR system using Cu/PPy and Cu/PTh.

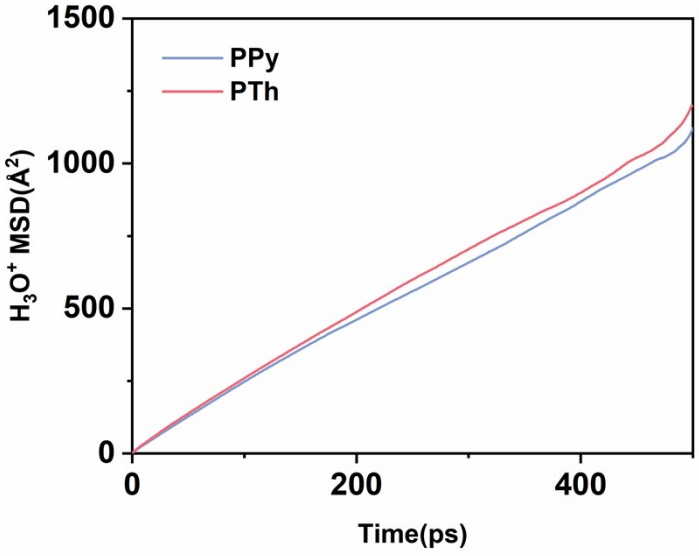

Fig. S26 MSD of the hydronium ion in the eCO_2RR system using Cu/PPy and Cu/PTh.

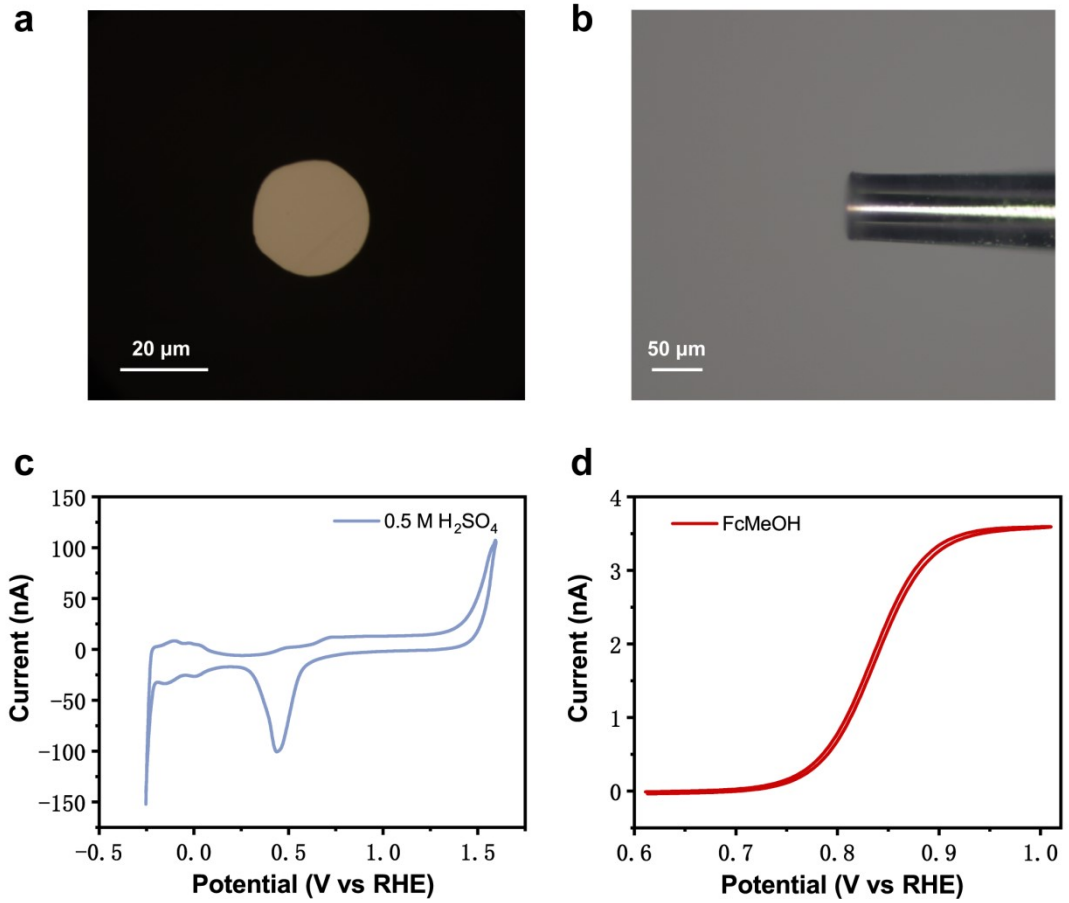

Fig. S27 (a) Top view and (b) side view of optical microscope images of Pt-UME; (c) Blank voltammetry of the polished Pt-UME used to perform the experiments taken in 0.5 M H_2SO_4 at the scan rate of 0.1 V s^{-1}; (d) CV of the steady-state current of Pt-UME obtained in 0.9 mM FcMeOH and 0.1 M KCl at the scan rate of 0.005 V s^{-1}.

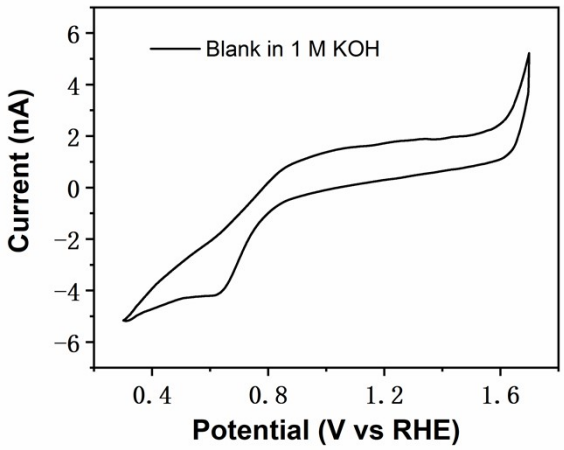

Fig. S28 Blank voltammogram of the Pt-UME in CO_2-saturated 1 M KOH at the scan rate of 0.05 V s^{-1}. No oxidation peaks of CO and H_2 were observed.

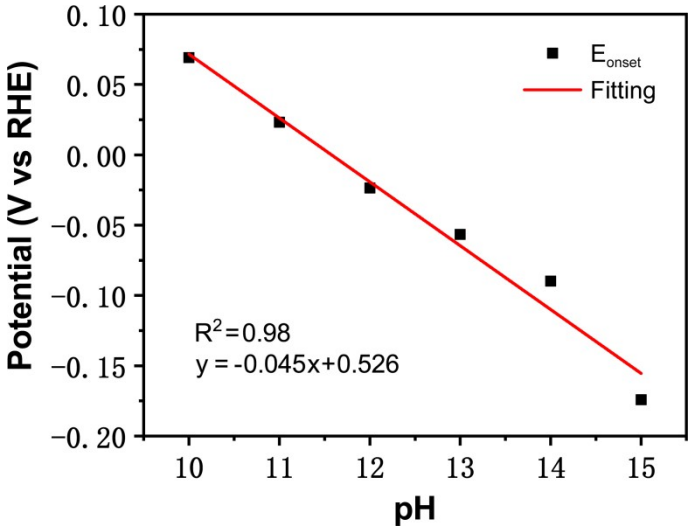

Fig. S29 The standard curve of local pH and HER E_{onset} in different pH solutions. The E_{onset} and pH are linearly related, suggesting that local pH can be obtained from changes in E_{onset}.

Table S1 Loadings of Cu_x/PPy composites

Sample	$CuCl_2 \cdot 2H_2O$ (mg)	Theoretical load of Cu (wt%)
PPy	0	0
Cu_{20}/PPy	26.732	20
Cu_{30}/PPy	46.018	30
Cu_{40}/PPy	71.549	40
Cu_{50}/PPy	107.323	50
Cu_{60}/PPy	160.986	60

Table S2 Quantification of Cu wt% by ICP-OES of Cu_x/PPy and Cu_x/PTh composites

Sample	Cu (wt%)
Cu_{20}/PPy	21.93
Cu_{30}/PPy	28.97
Cu_{40}/PPy	**48.76**
Cu_{60}/PPy	69.80
Cu_{80}/PPy	83.97
Cu_{20}/PTh	30.37
Cu_{40}/PTh	**51.47**
Cu_{60}/PTh	88.1

Table S3 Comparison of eCO_2RR performance of related samples

Samples	System	FE of C_{2+} (%)	Current density (mA/cm^2)	Ref.
Cu/PPy	Flow-cell	80.0	700	This work
Cu-Cu_2O-1	H-cell	80.0	11.5	[14]
Cu(B)-2	H-cell	79.0	70.0	[15]
Cu/Cu_2O@NG-2	H-cell	56.0	19.0	[16]
Cu HoMSs	Flow-cell	77.0	667	[17]
Cu-TABQ	Flow-cell	63.2	423	[18]
$Cu_2P_2O_7$	Flow-cell	73.6	350	[19]
h-Cu_2O ONS	Flow-cell	71.1	200	[20]
$Pd^{\delta-}$-Cu_3N	Flow-cell	78.2	116	[21]
Cu_3N_x	Flow-cell	81.7	307	[22]
Cu_2O-Ag	Flow-cell	72.8	243	[23]
Cu_2O/ILGS-400	Flow-cell	78.5	123	[24]
Nanoporous Cu	Flow-cell	62.0	653	[25]

References

1. B. E. Perdew, *Phys. Rev. Lett.*, 1996, **77**, 3865-3868.
2. B. W. Perdew, *Phys. Rev., B Condens. Matter.*, 1996, **54**, 16533-16539.
3. Blochl, *Phys. Rev., B Condens. Matter.*, 1994, **50**, 17953-17979.
4. G. J. Kresse, D, *Phys. Rev., B Condens. Matter.*, 1999, **59**, 1758-1775.
5. Z. Chen, X. Liu, J. Zhao, Y. Jiao and L. Yin, *J. Mater. Chem. A*, 2020, **8**, 11986-11995.
6. C. Li, Y. Liu, X. Le, Y. Yu, Q. Gong, F. Yang and J. Xie, *J. Electrochem. Soc.*, 2020, **167**.
7. H. Sun, Z. Sun and Y. Wu, *Int. J. Hydrogen Energy*, 2012, **37**, 12821-12826.
8. M. Rahmati, H. Modarress and R. Gooya, *Polymer*, 2012, **53**, 1939-1950.
9. S. Pahari, C. K. Choudhury, P. R. Pandey, M. More, A. Venkatnathan and S. Roy, *J. Phys. Chem. B*, 2012, **116**, 7357-7366.
10. S. H, *J. Phys. Chem. B*, 1998, **102**, 7338-7364.
11. K. Golzar, S. Amjad-Iranagh, M. Amani and H. Modarress, *J. Membr. Sci.*, 2014, **451**, 117-134.
12. J. Yana, P. Nimmanpipug, S. Chirachanchai, R. Gosalawit, S. Dokmaisrijan, S. Vannarat, T. Vilaithong and V. S. Lee, *Polymer*, 2010, **51**, 4632-4638.
13. T. Ohkubo, K. Kidena, N. Takimoto and A. Ohira, *J. Mol. Model*, 2011, **17**, 739-755.
14. Q. Zhu, X. Sun, D. Yang, J. Ma, X. Kang, L. Zheng, J. Zhang, Z. Wu and B. Han, *Nat. Commun.*, 2019, **10**, 3851.
15. Y. Zhou, F. Che, M. Liu, C. Zou, Z. Liang, P. De Luna, H. Yuan, J. Li, Z. Wang, H. Xie, H. Li, P. Chen, E. Bladt, R. Quintero-Bermudez, T. K. Sham, S. Bals, J. Hofkens, D. Sinton, G. Chen and E. H. Sargent, *Nat. Chem.*, 2018, **10**, 974-980.
16. W.-Y. Zhi, Y.-T. Liu, S.-L. Shan, C.-J. Jiang, H. Wang and J.-X. Lu, *J. CO2 Util.*, 2021, **50**.
17. C. Liu, M. Zhang, J. Li, W. Xue, T. Zheng, C. Xia and J. Zeng, *Angew. Chem. Int. Ed.*, 2022, **61**, e202113498.
18. F. Zhang, P. Wang, R. Zhao, Y. Wang, J. Wang, B. Han and Z. Liu, *ChemSusChem*, 2022, **15**, e202201267.
19. J. Sang, P. Wei, T. Liu, H. Lv, X. Ni, D. Gao, J. Zhang, H. Li, Y. Zang, F. Yang, Z. Liu, G. Wang and X. Bao, *Angew. Chem. Int. Ed.*, 2022, **61**, e202114238.
20. M. Jun, C. Kwak, S. Y. Lee, J. Joo, J. M. Kim, D. J. Im, M. K. Cho, H. Baik, Y. J. Hwang, H. Kim and K. Lee, *Small Methods*, 2022, **6**, e2200074.
21. Z. Zhang, S. Chen, J. Zhu, C. Ye, Y. Mao, B. Wang, G. Zhou, L. Mai, Z. Wang, X. Liu and D. Wang, *Nano Lett*, 2023, **23**, 2312-2320.
22. C. Peng, G. Luo, Z. Xu, S. Yan, J. Zhang, M. Chen, L. Qian, W. Wei, Q. Han and G. Zheng, *Adv Mater*, 2021, **33**, e2103150.
23. D. Niu, C. Wei, Z. Lu, Y. Fang, B. Liu, D. Sun, X. Hao, H. Pan and G. Wang, *Molecules*, 2021, **26**.
24. W. Wang, Z. Ma, X. Fei, X. Wang, Z. Yang, Y. Wang, J. Zhang, H. Ning, N. Tsubaki and M. Wu, *Chem. Eng. J.*, 2022, **436**.
25. J. J. Lv, M. Jouny, W. Luc, W. Zhu, J. J. Zhu and F. Jiao, *Adv. Mater.*, 2018, **30**, e1803111.